Journal Pre-proof



Spatial Proteomics Uncovers Immune Cell Neighborhoods and Tumor-Immune Interfaces in Pancreatic Ductal Adenocarcinoma

Jason Yeung, Yunhao Bai, Huaying Qiu, Yao Yu Yeo, Yuzhou Chang, Melissa S.F. Ng, Lara Rosaline Heij, Enas Abu Shah, Qin Ma, David Reiss, Garry Nolan, Shivan Sivakumar, Sizun Jiang

PII: S1535-9476(26)00193-3

DOI: https://doi.org/10.1016/j.mcpro.2026.101697

Reference: MCPRO 101697

To appear in: *Molecular & Cellular Proteomics*

Received Date: 14 April 2025

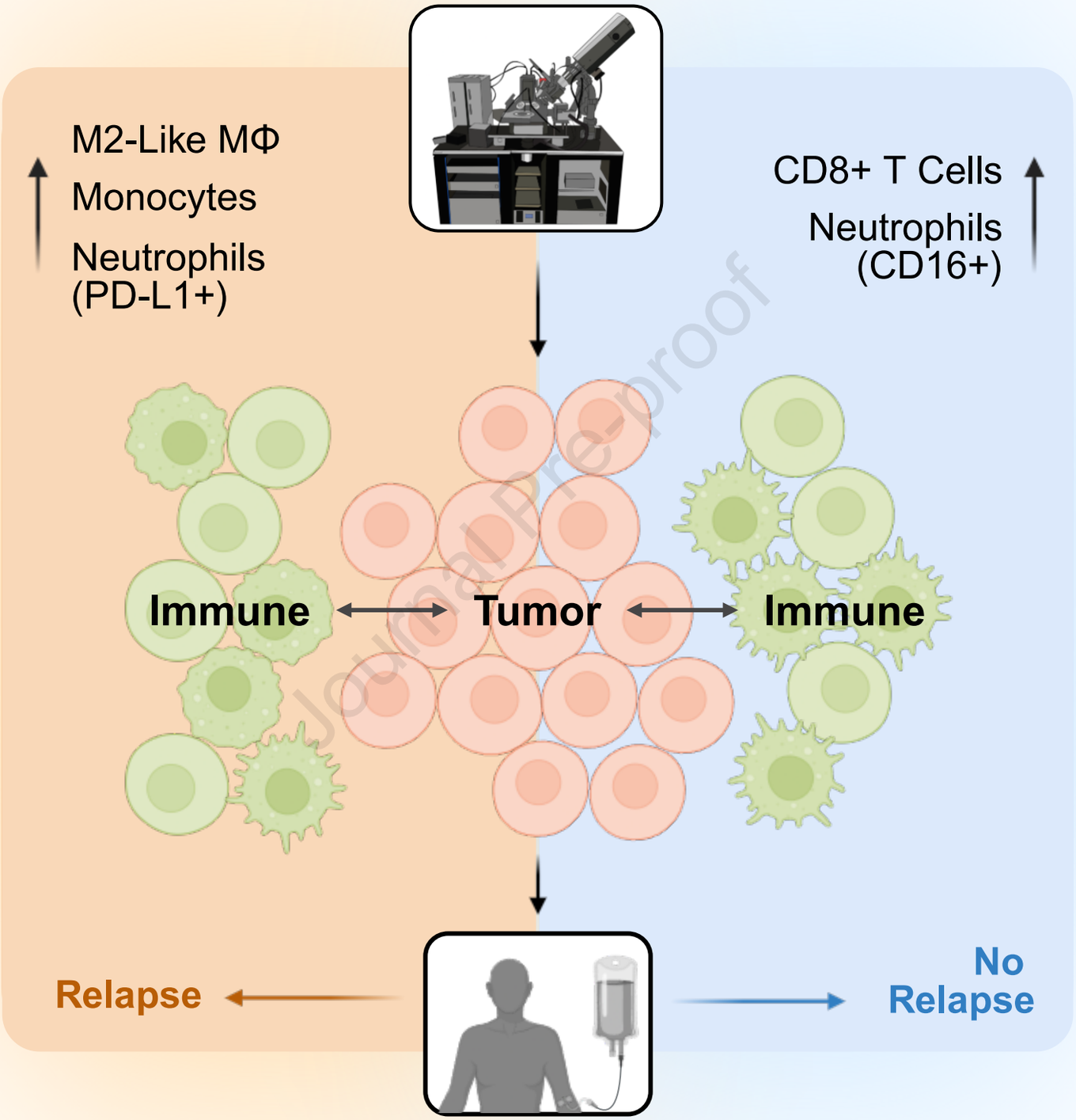
Revised Date: 23 October 2026

Accepted Date: 25 October 2026

Please cite this article as: Yeung J, Bai Y, Qiu H, Yeo YY, Chang Y, Ng MSF, Heij LR, Shah EA, Ma Q, Reiss D, Nolan G, Sivakumar S, Jiang S, Spatial Proteomics Uncovers Immune Cell Neighborhoods and Tumor-Immune Interfaces in Pancreatic Ductal Adenocarcinoma, *Molecular & Cellular Proteomics* (2026), doi: https://doi.org/10.1016/j.mcpro.2026.101697.

This is a PDF of an article that has undergone enhancements after acceptance, such as the addition of a cover page and metadata, and formatting for readability. This version will undergo additional copyediting, typesetting and review before it is published in its final form. As such, this version is no longer the Accepted Manuscript, but it is not yet the definitive Version of Record; we are providing this early version to give early visibility of the article. Please note that Elsevier's sharing policy for the Published Journal Article applies to this version, see: https://www.elsevier.com/about/policies-and-standards/sharing#4-published-journal-article. Please also note that, during the production process, errors may be discovered which could affect the content, and all legal disclaimers that apply to the journal pertain.

© 2026 THE AUTHORS. Published by Elsevier Inc on behalf of American Society for Biochemistry and Molecular Biology.



Journal Pre-proof

Journal Pre-proof

Spatial Proteomics Uncovers Immune Cell Neighborhoods and Tumor-Immune Interfaces in Pancreatic Ductal Adenocarcinoma

Jason Yeung[1,*], Yunhao Bai[2,3,*], Huaying Qiu[1], Yao Yu Yeo[1,4], Yuzhou Chang[1,5], Melissa S. F. Ng[6], Lara Rosaline Heij[7,8,9.10], Enas Abu Shah[11], Qin Ma[5], David Reiss[12], Garry Nolan[13], Shivan Sivakumar[14,15,#], Sizun Jiang[1,2,4,16,17,#]

Affiliations & Notes

1 Center for Virology and Vaccine Research, Beth Israel Deaconess Medical Center, Harvard Medical School, Boston, MA, United States

2 Broad Institute of MIT and Harvard, Boston, MA, United States

3 Department of Stem Cell and Regenerative Biology, Harvard University, Boston, MA, United States

4 Program in Virology, Division of Medical Sciences, Harvard Medical School, Boston, MA, United States

5 Pelotonia Institute for Immuno-Oncology, The James Comprehensive Cancer Center, The Ohio State University, Columbus, OH, USA

6 Singapore Immunology Network (SIgN), Agency for Science, Technology and Research (A∗STAR), Singapore, Republic of Singapore

7 Department of General, Visceral and Transplantation Surgery, Universitats Klinikum Essen, Essen, Germany.

8 Department of Pathology, Erasmus University Medical Center, Rotterdam, The Netherlands.

9 Institute of Experimental Medicine and Systems Biology, RWTH Aachen University, Aachen, Germany.

10 Institute of Pathology, University Hospital Essen, Essen, Germany

11 Kennedy Institute of Rheumatology, & Dunn School of Pathology, University of Oxford, Oxford, United Kingdom

Journal Pre-proof

Journal Pre-proof

12 Informatics and Predictive Sciences, Bristol Myers Squibb, Seattle, WA, United States

13 Department of Pathology, Stanford University, Stanford, CA, United States

14 Department of Immunology and Immunotherapy, School of Infection, Inflammation and Immunology, College of Medicine and Health, University of Birmingham, Birmingham, UK

15 Department of Oncology, Queen Elizabeth Hospital, University Hospitals of Birmingham NHS Trust, Mindelsohn Way, Birmingham, UK

16 Department of Pathology, Brigham and Women's Hospital, Harvard Medical School, Boston, MA, United States

17 Department of Pathology, Dana Farber Cancer Institute, Boston, MA, United States

* Co-first authors

Co-senior authors. Correspondence to s.sivakumar@bham.ac.uk or sjiang3@bidmc.harvard.edu

Running title: Spatial Proteomics Uncovers Tumor-Immune Interfaces in PDAC

Abbreviations

PDAC: Pancreatic ductal adenocarcinoma;

TME: Tumor microenvironment;

MIBI: Multiplexed ion beam imaging;

FFPE: Formalin-fixed paraffin-embedded;

Tregs: Regulatory T-cells;

PCA: Principal component analysis;

CN: Cell neighborhood;

Journal Pre-proof

Journal Pre-proof

Abstract

Pancreatic ductal adenocarcinoma (PDAC) remains one of the most lethal malignancies with dismal prognosis and limited treatment options. The complex interplay between tumor cells and their microenvironment contributes significantly to treatment resistance, yet technological challenges have hindered comprehensive spatial characterization of immune components in PDAC tissues. Here, we performed high-dimensional spatial proteomics using multiplexed ion beam imaging (MIBI) to quantify 27 protein markers across tissues from twelve treatment-naïve PDAC patients who subsequently underwent adjuvant chemotherapy. We achieved confident single-cell phenotypic mapping of the PDAC ecosystem through deep-learning based segmentation and expert-validated phenotypic annotation. Our analysis revealed significant enrichment of immunosuppressive myeloid populations in patients who eventually experienced disease relapse. Conversely, cytotoxic CD8+ T cells were depleted in these relapse-prone tumors. Using spatial probabilistic topic modeling, we identified eight distinct cellular neighborhoods with unique compositions and functional states, including the enrichment of an immune suppressive neighborhood in relapsed patients. While immunogenic cell neighborhoods were present in both patient populations, analysis of the tumor-immune neighborhoods demonstrated altered functional marker expression profiles, suggesting distinct immune activation in patients who relapsed versus those who did not. Our findings provide a high-resolution spatial atlas of the PDAC immune landscape and identify prognostic microenvironmental signatures that may inform the development of novel immunotherapeutic strategies for this recalcitrant disease.

Introduction

Pancreatic ductal adenocarcinoma (PDAC) composes the vast majority of pancreatic cancer cases, exhibits a five year survival rate below 10%, and is often treated with palliative

Journal Pre-proof

chemotherapy (1–3). While immunotherapy approaches have seen widespread success treating several types of cancer, anti-PD1 and anti-CTLA4 therapies have shown little to no benefit in PDAC to date (4–6). This lack of response initially suggested limited immune infiltration in the PDAC tumor microenvironment (TME); however, growing evidence now demonstrates significant immune cell presence within these tumors, prompting expanding efforts to characterize these populations to help develop more effective therapeutic strategies.

Our group and others have contributed towards characterizing the immune infiltrate (7–10), including demonstrating that prognosis can be determined by the amount of infiltrating lymphocytes in the resection specimen (8). Within tumor infiltrating lymphocytes, we further observed limited exhaustion in a subset of CD8 T cells, and that the majority of CD8 and CD4s were senescent (7, 9). We additionally demonstrated activated regulatory T-cells (Tregs) expressing multiple checkpoint molecules, including TIGIT, ICOS, CTLA4 and CD39, suggesting the presence of an immunosuppressive microenvironment (7, 9). Recent efforts in charting the single cell immune atlas of infiltrating immune cells in PDAC further unraveled the complexities of the immune cells present in the disease (10–14). While these studies have provided crucial insights into the phenotypic and functional characteristics of immune cells in PDAC, they largely lack the spatial context necessary to understand the complex cellular interactions that shape anti-tumor immunity. The spatial organization of immune cells relative to tumor cells and stromal elements has profound implications for their function, with proximity to tumor cells, exclusion by fibrotic barriers, and formation of tertiary lymphoid structures all potentially influencing therapeutic response (15). Additionally, distinct immune microenvironments may coexist within the same tumor, creating regional heterogeneity that cannot be captured by bulk or single-cell approaches alone. To address these critical knowledge gaps, we employed multiplexed ion beam imaging (MIBI) (16) to visualize 27 protein markers in PDAC tissues simultaneously, enabling comprehensive spatial mapping of immune cell phenotypes, functional states, and their relationships to clinical outcomes.

Journal Pre-proof

Experimental procedures

Human tissue acquisition and patient consent

Patients who underwent a curative resection for pancreatic ductal adenocarcinoma were consented for this study. Eight patients were recruited from Oxford under the Oxford Radcliffe biobank (09/H0606/5 + 5, project: 19/A177, REC: NRES Committee South Central - Oxford C). Four patients were recruited from Aachen medical centre under RWTH Aachen biobank project: EK360/19. Informed consent was obtained for all patients. The study was in strict compliance with all institutional ethical regulations. All tumor samples were surgically resected primary pancreatic ductal adenocarcinomas, and subsequently processed into formalin-fixed paraffin-embedded (FFPE) tissue blocks. All tumors were subjected to pathological re-review and histological confirmation by two expert PDAC pathologists before analysis. Individual clinical information used in this study can be found in **Supplementary Table 1** and is also referenced in Sivakumar et al. (10).

MIBI Antibody conjugation and panel

Antibody conjugation was performed using the Maxpar X8 Multimetal Labeling Kit (Fluidigm, 201300) and Ionpath Conjugation Kits (Ionpath, 600XXX) with a similar protocol as previously reported (17). Briefly, with a 50 kDa Amicon Ultra Filter (Millipore Sigma, UFC505096) as the reservoir, 100 µg of BSA-free was first washed quickly with buffer for conjugation reaction, then reduced with TCEP for 30 min in a 37 ℃ water bath at a final concentration of 4 µM (Thermo Fisher Scientific, 77720). After washing to remove excessive TCEP, the reduced antibody was mixed and incubated with lanthanide-loaded polymers for 90 min in a 37 ℃ water bath. Then, the product was washed five times with wash buffer and quantified using a NanoDrop (Thermo Scientific, ND-2000) in IgG mode at 280 nm. The concentration of products was then adjusted

to an easy-to-use number with at least 30% v/v Candor Antibody Stabilizer (Thermo Fisher Scientific, NC0414486), then stored at 4°C until staining. The MIBI panel for this study consisted of antibodies targeting PDAC-specific markers, stromal components, and immune cell markers to comprehensively analyze the pancreatic tumor microenvironment For more details regarding the antibodies used in this study, see **Supplementary Table 2**.

Tissue staining

The FFPE blocks of patient samples were sectioned at 4 μm thickness and mounted on the MIBIscope slides (Ionpath, #567001). MIBI staining was performed as previously described (18–21). Briefly, the slides with FFPE sections were first baked at 70°C for 90 min, followed by antigen retrieval at 95°C for 20 min with Target Retrieval Solution (Agilent, S236784-2) on a PT Module (Thermo Fisher Scientific, A80400012). The section was then blocked by BBDG (5% normal donkey serum, 0.05% NaN_3 in 1x TBS-T) and stained with a cocktail of conjugated antibodies at 4°C overnight. Subsequently, the sample was washed with wash buffer (0.1% BSA in 1x TBS-T) and post-fixed with 4% PFA and 2% glutaraldehyde in 1x PBS, before undergoing a series of dehydration steps on the linear stainer (3x with 100 mM Tris pH 7.5, 3x with ddH_2O, 1x with 70% EtOH, 1x with 80% EtOH, 2x with 95% EtOH, 3x with 100% EtOH, 180 s for each wash), before storage in a vacuum desiccator until acquisition. The panel and concentration of each antibody can be found in **Supplementary Table 2**.

MIBI image acquisition and pre-processing

The multiplexed image datasets of MIBI were acquired using a commercially available MIBIscope™ system from Ionpath. In addition to the built-in quality control, the beam current was measured and adjusted using a Faraday cup before each run to ensure it fell within the recommended range. A quick scan of a Molybdenum foil target was then performed, and the

Journal Pre-proof

count yields of Molybdenum isotopes were recorded to confirm proper ion detection. Except the built-in quality control, before every run, the beam current was measured and adjusted over a Faraday cup to be located within the recommended range; then, a quick run over a Molybdenum foil target was performed, and counts yields of Molybdenum isotopes were noted to assure good ion detection. For real runs, the field of view (FOV) acquired and the parameters used for each FOV can be found in **Supplementary Table 3**, with typical conditions listed as below:

- Pixel dwell time: 2 ms
- Image area: 400 × 400 μm
- Image size: 512 × 512 pixels
- Probe size: ~400 nm
- Primary ion current: Coarse mode (9.5-10 nA on a built-in Faraday cup)
- Number of planes: 1 depth
- Time cost per image: 8.5 min

Specifically, due to the rather limited FOVs area that MIBI is able to acquire at scale, a board-certified pathologist (L.R.H.) first selected the FOVs of pathological interest (focusing on tumor and immune infiltrates) from the accompanying sequential H&E sections. These FOVs were subsequently acquired by MIBI.

After the raw .bin files were generated by the MIBIscope machine, the single-channel mass spectrometry images were extracted using the toffy package (v0.2.2) https://github.com/angelolab/toffy (22). The mass range for extraction of each channel can be found in **Supplementary Table 2**. Imaging stitching was performed with custom MatLab scripts (https://github.com/dtebaykin/MibiStitch) followed by flat-field correction. MIBI data often contains several sources of background noise, including gold ions from the conductive slide, isotopic impurities, and elemental contamination. To systematically correct for any sources of contamination, we performed Rosetta image compensation using toffy v0.2.2

(https://github.com/angelolab/toffy/) (22). Coefficients for sources of noise spillover were empirically determined using a grid search method to remove noise while retaining biological signal.

Single Cell Segmentation and Expression Matrix Extraction

Cell segmentation was performed using Mesmer (v0.12.2) (23) with the following parameters:

- Nucleus channel: Histone H3
- Membrane channels: sum of channel HLA-DR, CD45-RA, CD3, CD20, CD68
- Mpp = 0.78,
- interior_threshold = 0.05
- maxima_threshold = 0.075

The signals of all markers within each segmented cell area were summed and then normalized by the cell size, to create a final cell expression matrix in which each row represents a single cell. Each column represents the size-normalized expression level of different markers. We next perform a percentile cutoff at 0.5% (floor) and 99.5% (ceiling) for each marker, before scaling the final expression to 0-1. This final cell expression matrix was used for the rest of the analysis. Additional processed data information can be found in the **Data Availability** section.

Cell Type Annotation, Clustering, Neighborhood Modeling

Using the final cell expression matrix generated as described above, initial cell clusters were identified using PhenoGraph [v0.99.1] (24). Clusters were manually assigned putative cell type identities based on canonical phenotypic marker expression, before visual validation by plotting back the phenotypes to the multiplexed MIBI image. Further subclustering was performed as needed iteratively. Final tumor cell populations were manually distinguished from normal epithelial cell populations with the guidance and expertise from a certified pathologist (L.R.H)

Journal Pre-proof

Journal Pre-proof

using MIBI images and the accompanying H&E scans from a sequential section. All final staining and annotations were visually validated by L.R.H.

Cell neighborhoods were identified across tissue regions using Spatial-LDA (25) with parameter admm_rho = 0.1. The model was fitted with $n \in \mathbf{N} = \{6, 7, 8, 10, 11\}$ neighborhoods before identifying $n = 8$ as the optimal number of neighborhoods with maximum resolution and legibility (**Fig. S3A**). Cells interfacing at the borders of cell neighborhoods were determined via Delaunay triangulation using deldir (2.0.4). Codes that used to generate each figure can be found in the Data Availability section.

Cancer Buffering Zone Analysis

To extract the tumor patches in the PDAC image, the mix_keratin MIBI images were binarized, morphologically transformed, and size filtered to generate epithelial patches images. After that, the pathologist-guided tumor annotations from L.R.H. were used to identify whether those patches were cancerous, to generate tumor patch maps for each FOV.

The tumor-cell-distance was then generated for every cell of each FOV by looping through each cell and measuring the distance between it and the closest tumor patches. The cells were then binned together based on distance for subsequent visualization. Codes that used to generate each figure can be found in the Data Availability section.

Statistical Modeling

In order to have a comprehensive view of effects of the functional profile of the neutrophils on patient response (relapse vs. non-response) and its interaction with the spatial location of associated neutrophils either near or far from tumor, a modeling approach with principal component analysis (PCA) and random forest was implemented with 10 repeated 3-fold cross validation where each fold was stratified at patient level.

Journal Pre-proof

Neutrophils were first categorized into “near tumor” (≤25 μm from the closest tumor area) and “far from tumor” (>25 μm but ≤100 μm). Then PCA was performed on the each group’s functional profile (CD16, MPO, CD45RA, CD45RO, HLA-DR, Ki-67, PD-L1) to get two sets of principle components, one for the near tumor profile and the other for the far from tumor profile. Then these PCs were used to fit random forest models with relapse status as the response variable. 10 repeated 3-fold cross validation was used to get more robust estimates.
The variable importance metrics for each model were recorded and the PCs were ranked based on their frequency of being the top 5 most important variables in a model. Then, the top PCs were picked and their loadings were inspected to determine the biological interpretation of the PCs. Codes used to generate each figure can be found in a Github repository under the Data Availability section.

Power Calculation

To identify relapse-associated differences, we first quantified the relative abundance of each cell type and cell neighborhood (CN) within every FOV or non-overlapping sub-FOVs. For each sub-FOV, the proportion of a given cell type or CN was calculated by dividing its cell count by the total number of cells in that sub-FOV. These proportions were then compared between relapse and non-relapse groups using the two-sided Wilcoxon rank-sum test, a non-parametric method suitable for non-normally distributed data. Statistical significance was determined at a threshold of $\alpha=0.05$, and fold differences were expressed as log2-transformed ratios between the mean proportions of the two groups. To assess the robustness of these findings under limited sample size, we conducted an empirical simulation-based power analysis (26–28). An equal number of non-overlapping sub-FOVs were randomly dropped from the relapse and non-relapse groups across 200 iterations, and the Wilcoxon test was repeated at each iteration. This stratified subsampling strategy allowed us to estimate the empirical probability of detecting significant

Journal Pre-proof

differences ($p < 0.05$) across a series of reduced-sample scenarios. The resulting empirical power was summarized as the proportion of iterations in which significance was retained, and 95% confidence intervals were computed using binomial estimates (29). This simulation-based approach accounts for biological heterogeneity and spatial sampling variability, providing a realistic measure of statistical stability under the current cohort size. Consistently high empirical power (≥80%) across multiple subsampling levels indicates that the observed relapse-associated cellular and spatial features are reproducible and not driven by overfitting.

Results

Spatial immune profiling reveals distinct immune signatures in pancreatic adenocarcinoma

To elucidate the key immune determinants that drive this treatment resistance and disease recurrence, we conducted a prospective study of 12 treatment-naïve PDAC patients who subsequently underwent adjuvant chemotherapy (**Fig. 1A**). At the time of this analysis, 8 patients had experienced cancer relapse while 4 patients remained relapse-free, providing a rare opportunity to identify potential pre-treatment immune signatures associated with clinical outcomes.

To interrogate the tumor immune landscape at single-cell resolution, we employed multiplexed ion beam imaging (MIBI) using a comprehensive 27-marker panel. This panel captured key lymphoid, myeloid, and stromal phenotype markers, alongside functional markers indicative of cell activation and exhaustion states (**Fig. 1B, Fig. S1A**). By integrating MIBI with advanced single-cell segmentation and annotation algorithms, we were able to resolve distinct cell phenotypes and their spatial relationships within the preserved tissue architecture This approach enabled simultaneous visualization and quantification of tumor cells, diverse immune

Journal Pre-proof

populations, and their functional states within the intact tumor microenvironment (**Fig. 1C, Fig. S2A**). 39 multiplexed images were acquired on regions of interest with MIBIscope under the guidance of a board-certified pathologist using the H&E scan from the sequential section **(Fig. 1D)**.

Recurrent pancreatic tumors are enriched with immune-suppressive myeloid cell populations

To characterize the cellular composition of the PDAC tumor microenvironment, we performed unsupervised clustering of cellular marker expression profiles across all tissue samples. This analysis identified 16 distinct cell populations, including multiple T cell subsets, B cells, macrophages with diverse phenotypic states, as well as non-immune stromal and epithelial components (**Fig. 2A, Fig. S2B**). The clustering results exhibited clear delineation between lymphoid and myeloid lineages, while also capturing functional heterogeneity within these major lineages. This diverse panel enabled the further delineation of cell populations based on their proliferative capacity (Ki67), immune checkpoint expression (PD-1, PD-L1), and activation status (CD25, ICOS) (**Fig. 2B**).

When comparing samples from patients who experienced disease relapse to those who remained relapse-free, we observed a striking enrichment of immunosuppressive myeloid populations in the relapse group (**Fig. 2C, Fig. S3A**). Comparative enrichment analysis revealed that macrophages exhibiting an M2-like, anti-inflammatory phenotype and normal epithelial cell populations were the most significantly enriched in treatment-naive samples from relapsed patients. This enrichment pattern extended to monocytes as well, suggesting a broadly immunosuppressive microenvironment in tumors prone to recurrence. In contrast, cytotoxic CD8+ T cells were significantly depleted in the relapse group before treatment, indicating

compromised anti-tumor immunity in these patients and confirming the presence of cytotoxic T cells as a strong indicator of tumor clearance (30). Importantly, these cellular composition differences were consistently observed across individual patients, reinforcing the robustness of this immunosuppressive signature as a potential determinant of treatment response (**Fig. 2D**). We postulated that the relatively small sample size may pose challenges to the robustness of the findings. To our knowledge at the time of this study, no publicly available PDAC multiplex imaging dataset includes explicit relapse versus relapse-free annotations, which precludes external validation. To address this limitation, we implemented a simulation-based empirical power analysis to assess the reproducibility of the observed phenotypic differences within the existing dataset. Specifically, each field of view (FOV) was divided into 20 non-overlapping sub-FOVs to increase the number of statistically independent sampling units while avoiding pseudo-replication. We then conducted a stratified random subsampling experiment, in which an equal number of sub-FOVs were randomly dropped from both relapse and non-relapse groups at each iteration (200 iterations per drop level). For every cell type, a Wilcoxon rank-sum test was recalculated, and empirical power was defined as the proportion of iterations where $p < 0.05$, with 95% binomial confidence intervals.

As shown in the Figure S3A, several immune and epithelial cell populations maintained ≥ 80% statistical power even after random subsampling, indicating robust and reproducible group differences. Notably, neutrophils retained high empirical power even after 100~150 sub-FOVs were dropped from each group, demonstrating that the neutrophil phenotype remains statistically stable under reduced sampling. Similar stability was observed for CD4 T cells, CD8 T cells, epithelial cells, lymphatic cells, M2-like macrophages, monocytes, and plasmablasts, which collectively support the biological robustness of the relapse-associated immune signatures. This empirical scaling analysis provides an internal validation framework that mimics testing across smaller, hypothetical cohorts and demonstrates that the key neutrophil and immune cell patterns are not artifacts of limited sampling.

Journal Pre-proof

Spatial organization reveals neighborhoods of immune suppression associated with patient relapse

Beyond individual cell populations, the spatial organization of immune cells and their interactions within the tumor microenvironment may critically influence disease progression. To characterize these spatial patterns, we implemented a probabilistic topic modeling approach that defined distinct tissue multicellular structures, which we term "cellular neighborhoods" (**Fig. 3A, Fig. S3B**). This unsupervised analysis identified eight distinct neighborhood types, each with a unique cellular composition and spatial arrangement.

Marker expression analysis within these neighborhoods revealed coordinated patterns of immune modulation that transcended individual cell types, suggesting emergent properties of cellular communities (**Fig. 3B**). We identified an "immune suppressive" neighborhood characterized by co-localization of M2-like macrophages and monocytes. Interestingly, we also identified a neighborhood dominated by normal epithelial cells with Ki67 expression, suggesting potential abnormal proliferation. Both neighborhood types were significantly enriched in relapse-positive patients and may potentially play a role in enabling tumorigenesis and tumor recurrence (**Fig. 3C**, **Fig. S3C**).

To further characterize tumor-immune interactions, we constructed an Euclidean distance matrix to measure the proximity between cells within tumor neighborhoods and those in other neighborhood types (**Fig. 3D**). This spatial mapping revealed which immune modules were most frequently occupied at the tumor-immune interface. Complementing this analysis, we employed Delaunay triangulation, where edges represent direct cellular interactions, to quantify the proportion of tumor neighborhood cells directly interfacing with cells from different neighborhood types. The "active immune" and "immune rich" neighborhoods comprised the most frequent interactions with tumor regions in non-relapsed patients (**Fig. 3E**). Analysis of the functional marker profile of cells at these tumor-immune interfaces identified differential expression of

Journal Pre-proof

immune checkpoint and activation markers (**Fig. 3F**). At the “active immune” interface, cell populations expressed lower levels of CD11b, CD15, and CD16 myeloid and CD45RO, HLA-DR, and MPO immune activation markers, suggesting the presence of functionally distinct and potentially immunosuppressive cell states despite phenotypic similarity.

Tumor buffer zone analysis reveals distinct spatial distribution of immune cells and functional features of neutrophils associated with disease recurrence

A distance-based analysis was next performed to evaluate how different cell phenotypes are spatially distributed relative to tumor regions. By combining keratin staining with pathologist-annotated tumor areas, tumor masks were generated for each FOV. For each cell, the minimum distance to the tumor area was calculated (**Fig. 4A**), enabling precise spatial mapping of immune populations relative to the tumor boundary. Cell phenotype ratios were then binned based on their distance from the tumor, and plotted according to patient relapse status (**Fig. 4B, Fig. S4A**).

This spatial analysis revealed striking differences in the immune cell composition surrounding tumor regions between relapsed and non-relapsed patients. Neutrophils emerged as the most abundant and differentially distributed cell type near tumor regions in both patient groups, but with distinct distribution patterns and functional characteristics (**Fig. 4B**). In relapsed patients, we observed a concentrated zone of neutrophils immediately proximal tumor border, while non-relapsed patients showed increased neutrophil presence further away (>25um) from the immediate tumor interface (**Fig. 4B**).

Although the CD15 expression in the neutrophils was not significantly different across the relapsed and-non relapsed patients, functional markers showed significant differences between these two groups (**Fig. 4C**). Neutrophils in relapsed patients exhibited significantly higher

Journal Pre-proof

expressions of PD-L1, MPO, and lower CD45RO compared to those in non-relapsed patients (**Fig. 4C**). The PD-L1 expressing tumor-associated neutrophils (TANs) generally are considered as pro-tumor through suppression of cytotoxic T cells, and have been shown to contribute to the growth and progression of some human cancers (31, 32). Recent evidence also shows that the regulation towards the PD-1/PD-L1 axis blocks the neutrophil cytotoxicity in cancer (33). Those evidence may align with the elevated PD-L1 level in TANs of relapsed state patients. A preliminary report also demonstrated TANs-mediated immunosuppression depends on MPO-driven ROS, and knocking out or inhibiting MPO reduces suppression and slows tumor growth (34). Thus, these functional differences align with known features of TANs and suggest distinct neutrophil phenotypes associated with disease outcomes. While neutrophil populations grouped by proximity to the tumor (near vs. far) also exhibited functional differences, the contrast was more pronounced between relapse groups than between distance cohorts (**Fig. S4A&B**), indicating that at least in this context of these tumor-associated neutrophils, the functional state is more predictive than spatial organization for clinical outcome.

To further explore the association of neutrophils with patient relapse status, we next trained a random forest model using the features from tumor-associated neutrophils. Given the limited sample size (n = 12; relapsed = 8, non-relapsed = 4), we first applied principal component analysis (PCA) to reduce dimensionality. This analysis included features from neutrophil populations categorized as “near” (≤25 μm from the tumor border) and “far” (>25 μm but ≤100 μm) (**Fig. 4D**).

The model revealed consistent patterns showing that features from "near" neutrophil populations contributed more significantly to relapse than those from "far" populations (**Fig. S4C&D**). The partial dependence plots for key neutrophil populations highlighted the correlation between neutrophil characteristics and relapse probability (**Fig. S4E**), which is next visualized via the PCA loading matrix for the model (**Fig. 4E**). By integrating the PCA loading matrix with these partial dependence relationships, we identified that at least two distinct neutrophil

Journal Pre-proof

neutrophil-associated signatures are associated closely with the outcomes in PDAC patients (**Fig. 4F**). Specifically, features derived from populations 4 and 7 exhibited distinct PD-L1-associated patterns, differing in their relationships with CD45RO and CD16, respectively (**Fig. 4E&S4E**, summarized in **Fig. 4F**). Despite the nonmonotonic association observed for population 2, these findings suggest that distinct multivariate neutrophil-associated signatures may capture complementary information relevant to relapse prediction.

The targeted nature of the antibody-based imaging spatial proteomics also encompasses a lower number of features measured compared with methods such as scRNA-seq. Furthermore, tumour neutrophil subsets are frequently defined by scRNAseq-based clustering without definitive, empirical verification of associated surface markers, thus making it difficult to construct strict correlations between our neutrophil populations (identified with protein-based methods) with the established paradigms (35, 36). Nevertheless, an elevated level of PD-L1 in population 4 functionally suggests their correlation with the immunosuppressive TAN populations, or "N2" state. Their presence in the pre-treatment state could further enhance the immune suppressive PD-1/PD-L1 axis in the context of PDAC, resulting in suppression of anti-tumour T cell responses to drive potential relapse (33). On the other hand, CD16 expression in neutrophils marks mature neutrophils (37), and high CD16 expressing TANs with lower PD-L1 expression were more enriched in non-relapsed patients prior to treatment. These findings further emphasize the heterogeneity of TANs across PDAC patients, and imply the potential association between the functional polarization of neutrophils at the tumor-immune interface and treatment response and disease progression in PDAC.

Journal Pre-proof

Discussion

Our spatial proteomic profiling of pancreatic ductal adenocarcinoma has revealed insights into the complex tumor microenvironment that may underlie the poor response to conventional therapies and immunotherapeutic approaches. By integrating high-dimensional protein expression data with spatial information at the single-cell resolution, we have identified distinct cellular neighborhoods and immune cell functional states associated with disease recurrence following adjuvant chemotherapy.

Despite the highly immunosuppressive nature of PDAC, a key finding of our study is the further enrichment of immunosuppressive myeloid populations in patients who experienced disease relapse. The abundance of M2-like macrophages and specific monocyte populations suggests a coordinated immunosuppressive program that may facilitate tumor escape from immune surveillance. This observation aligns with previous studies highlighting the importance of myeloid-derived suppressor cells in PDAC progression (38, 39), and further extends beyond these findings by demonstrating their spatial organization relative to tumor cells and other immune populations.

Particularly striking was our discovery of neutrophil phenotypic heterogeneity at the tumor-immune interface. The distinct functional profiles of neutrophils in relapsed versus non-relapsed patients, characterized by differential expression of PD-L1, MPO, CD45RO, and CD16, points to the polarization of these cells as a potential determinant of disease outcome, and adds to the growing appreciation of neutrophil plasticity in cancer (40).

The spatial analysis of cellular neighborhoods revealed organized multicellular structures with distinct compositions and functional states that reflect differences in immune engagement. This pattern suggests that relapse is associated with diminished anti-tumoral immune function, despite phenotypically similar and “active” neighborhood architecture. This rationalizes the need

Journal Pre-proof

to include both spatial context and cellular features in developing robust predictors of treatment response in PDAC, as demonstrated in our proof of concept here.

Our study has several clinical implications. First, the identification of cellular neighborhoods associated with disease recurrence provides potential biomarkers for risk stratification. Patients with high infiltration of immunosuppressive myeloid cells, particularly with specific neutrophil phenotypes, might benefit from more aggressive treatment approaches or closer surveillance. Second, the functional heterogeneity of myeloid populations suggests potential targets for therapeutic intervention. Strategies to reprogram immunosuppressive myeloid cells toward pro-inflammatory phenotypes or selectively deplete specific subsets could enhance the efficacy of conventional chemotherapy or immunotherapy (36).

Several limitations of our study should be acknowledged. The relatively small sample size, while providing statistically significant results and validated by power calculation, can be damaging to the robustness of above clinical conclusion in light of the heterogeneity of PDAC, this study would benefit from future validation in larger, independent cohorts. Besides that, we did not include cancer-associated fibroblasts (CAFs) in our analysis, although they are key parts of the PDAC TME. While elevated levels of SMA, an established CAFs marker, can be robustly observed surrounding the malignant epithelial layers, the lack of a clear single lineage marker and difficulties in segmentation and annotation resulted in CAFs being grouped in the “Other” cell phenotype category. Additionally, while our multiplexed imaging approach provided detail of the PDAC microenvironment, integrating these findings with genomic alterations and systemic immune parameters in the future could provide a more comprehensive understanding of treatment response determinants.

Exciting future directions also include exploring the mechanisms driving the formation of distinct cellular neighborhoods in PDAC and investigating whether these spatial patterns change dynamically during treatment. Longitudinal sampling before and after treatment could provide insights into how cellular neighborhoods evolve during disease progression and treatment

resistance. Furthermore, functional studies are direly needed to determine whether targeting specific cellular neighborhoods could enhance therapeutic efficacy.

In conclusion, our spatial proteomic profiling of PDAC reveals a complex ecosystem of tumor and immune cells whose organization and functional states are associated with disease recurrence. The identification of specific cellular neighborhoods and myeloid cell phenotypes provides new insights into the mechanisms of treatment resistance and offers potential avenues for therapeutic intervention. The potential association between neutrophil subsets near the tumor boundary and the disease outcomes further underscores the importance of considering spatial context in understanding cancer biology, and highlights the potential of spatial proteomics as a powerful approach for dissecting the tumor microenvironment in PDAC and other cancer types.

CRediT authorship contribution statement

Jason Yeung: Writing – review & editing, Writing – original draft, Visualization, Validation, Methodology, Investigation, Formal analysis, Data curation. Yunhao Bai: Writing – review & editing, Writing – original draft, Visualization, Validation, Methodology, Investigation, Formal analysis, Data curation. Huaying Qiu: Writing – review & editing, Methodology, Formal analysis, Data curation. Yao Yu Yeo: Writing – review & editing, Methodology, Investigation. Yuzhou Chang: Writing – review & editing, Formal analysis. Melissa S. F. Ng: Writing – review & editing, Formal analysis. Lara Rosaline Heij: Writing – review & editing, Resources. Enas Abu Shah: Writing – review & editing, Resources. David Reiss: Writing – review & editing, Resources. Qin Ma: Writing - review & editing, Supervision, Resources. Garry Nolan: Supervision, Resources. Shivan Sivakumar: Writing – review & editing, Writing – original draft, Supervision, Resources, Funding acquisition, Conceptualization. Sizun Jiang: Writing – review & editing, Writing – original draft, Supervision, Resources, Funding acquisition, Conceptualization.

Journal Pre-proof

Journal Pre-proof

Disclosure

S.S. held a personal fellowship from BMS during this study with a grant provided to conduct experiments and also has research funding from Alchemab, has received speaker fees and travel grants from Astrazeneca, Novartis and Servier; and also conducts trials with Astrazeneca, Novartis, Roche, Genentech and BioNTech. S.J. is a co-founder of Elucidate Bio Inc, and serves on its Board of Directors and Scientific Advisory Board, and has received research support from Roche and Novartis unrelated to this work.
The authors declare no other competing interests.

Acknowledgement

S.J. is supported by in part by NIH DP2AI171139, U24CA224331, a Gilead's Research Scholars Program in Hematologic Malignancies, a Sanofi iAward, the Broad Next Generation Award, the Dye Family Foundation, and the Bridge Project, a partnership between the Koch Institute for Integrative Cancer Research at MIT and the Dana-Farber/Harvard Cancer Center.

Data availability

All the extracted .tiff files to assemble the multiplexed image acquired by MIBIscope are available on Zenodo doi: 10.5281/zenodo.15109931. Codes used to perform the analysis and generate figures are deposited to GitHub under http://github.com/SizunJiangLab/PDAC_MIBI.

Supplemental data

This article contains supplemental data.

Journal Pre-proof

Journal Pre-proof

Reference

1. Conroy, T., Castan, F., Lopez, A., Turpin, A., Ben Abdelghani, M., Wei, A. C., Mitry, E., Biagi, J. J., Evesque, L., Artru, P., Lecomte, T., Assenat, E., Bauguion, L., Ychou, M., Bouché, O., Monard, L., Lambert, A., Hammel, P., and Canadian Cancer Trials Group and the Unicancer-GI–PRODIGE Group (2022) Five-Year Outcomes of FOLFIRINOX vs Gemcitabine as Adjuvant Therapy for Pancreatic Cancer: A Randomized Clinical Trial. *JAMA Oncol* 8, 1571–1578

2. Von Hoff, D. D., Ervin, T., Arena, F. P., Chiorean, E. G., Infante, J., Moore, M., Seay, T., Tjulandin, S. A., Ma, W. W., Saleh, M. N., Harris, M., Reni, M., Dowden, S., Laheru, D., Bahary, N., Ramanathan, R. K., Tabernero, J., Hidalgo, M., Goldstein, D., Van Cutsem, E., Wei, X., Iglesias, J., and Renschler, M. F. (2013) Increased survival in pancreatic cancer with nab-paclitaxel plus gemcitabine. *N Engl J Med* 369, 1691–1703

3. Siegel, R. L., Miller, K. D., Wagle, N. S., and Jemal, A. (2023) Cancer statistics, 2023. *CA Cancer J Clin* 73, 17–48

4. O'Reilly, E. M., Oh, D.-Y., Dhani, N., Renouf, D. J., Lee, M. A., Sun, W., Fisher, G., Hezel, A., Chang, S.-C., Vlahovic, G., Takahashi, O., Yang, Y., Fitts, D., and Philip, P. A. (2019) Durvalumab With or Without Tremelimumab for Patients With Metastatic Pancreatic Ductal Adenocarcinoma: A Phase 2 Randomized Clinical Trial. *JAMA Oncol* 5, 1431–1438

5. Bockorny, B., Semenisty, V., Macarulla, T., Borazanci, E., Wolpin, B. M., Stemmer, S. M., Golan, T., Geva, R., Borad, M. J., Pedersen, K. S., Park, J. O., Ramirez, R. A., Abad, D. G., Feliu, J., Muñoz, A., Ponz-Sarvise, M., Peled, A., Lustig, T. M., Bohana-Kashtan, O., Shaw, S. M., Sorani, E., Chaney, M., Kadosh, S., Vainstein Haras, A., Von Hoff, D. D., and Hidalgo, M. (2020) BL-8040, a CXCR4 antagonist, in combination with pembrolizumab and chemotherapy for pancreatic cancer: the COMBAT trial. *Nat Med* 26, 878–885

6. Padrón, L. J., Maurer, D. M., O'Hara, M. H., O'Reilly, E. M., Wolff, R. A., Wainberg, Z. A., Ko, A. H., Fisher, G., Rahma, O., Lyman, J. P., Cabanski, C. R., Yu, J. X., Pfeiffer, S. M., Spasic, M., Xu, J., Gherardini, P. F., Karakunnel, J., Mick, R., Alanio, C., Byrne, K. T., Hollmann, T. J., Moore, J. S., Jones, D. D., Tognetti, M., Chen, R. O., Yang, X., Salvador, L., Wherry, E. J., Dugan, U., O'Donnell-Tormey, J., Butterfield, L. H., Hubbard-Lucey, V. M., Ibrahim, R., Fairchild, J., Bucktrout, S., LaVallee, T. M., and Vonderheide, R. H. (2022) Sotigalimab and/or nivolumab with chemotherapy in first-line metastatic pancreatic cancer: clinical and immunologic analyses from the randomized phase 2 PRINCE trial. *Nat Med* 28, 1167–1177

7. Sivakumar, S., Abu-Shah, E., Ahern, D. J., Arbe-Barnes, E. H., Jainarayanan, A. K., Mangal, N., Reddy, S., Rendek, A., Easton, A., Kurz, E., Silva, M., Soonawalla, Z., Heij, L. R., Bashford-Rogers, R., Middleton, M. R., and Dustin, M. L. (2021) Activated Regulatory T-Cells, Dysfunctional and Senescent T-Cells Hinder the Immunity in Pancreatic Cancer. *Cancers (Basel)* 13,

8. de Santiago, I., Yau, C., Heij, L., Middleton, M. R., Markowetz, F., Grabsch, H. I., Dustin, M. L., and Sivakumar, S. (2019) Immunophenotypes of pancreatic ductal adenocarcinoma: Meta-analysis of transcriptional subtypes. *Int J Cancer* 145, 1125–1137

9. Jainarayanan, A., Mouroug-Anand, N., Arbe-Barnes, E. H., Bush, A. J., Bashford-Rogers, R., Frampton, A., Heij, L., Middleton, M., Dustin, M. L., Abu-Shah, E., and Sivakumar, S. (2023) Pseudotime dynamics of T cells in pancreatic ductal adenocarcinoma inform distinct functional states within the regulatory and cytotoxic T cells. *iScience* 26, 106324

10. Sivakumar, S., Jainarayanan, A., Arbe-Barnes, E., Sharma, P. K., Leathlobhair, M. N., Amin, S., Reiss, D. J., Heij, L., Hegde, S., Magen, A., Tucci, F., Sun, B., Wu, S., Anand, N. M., Slawinski, H., Revale, S., Nassiri, I., Webber, J., Hoeltzel, G. D., Frampton, A. E., Wiltberger, G., Neumann, U., Charlton, P., Spiers, L., Elliott, T., Wang, M., Couto, S., Lila, T., Sivakumar, P. V., Ratushny, A. V., Middleton, M. R., Peppa, D., Fairfax, B., Merad, M., Dustin, M. L., Abu-Shah, E., and Bashford-Rogers, R. (2025) Distinct immune cell infiltration patterns in pancreatic ductal adenocarcinoma (PDAC) exhibit divergent immune cell selection and immunosuppressive mechanisms. *Nat Commun* 16, 1397

11. Hwang, W. L., Jagadeesh, K. A., Guo, J. A., Hoffman, H. I., Yadollahpour, P., Reeves, J. W., Mohan, R., Drokhlyansky, E., Van Wittenberghe, N., Ashenberg, O., Farhi, S. L., Schapiro, D., Divakar, P., Miller, E., Zollinger, D. R., Eng, G., Schenkel, J. M., Su, J., Shiau, C., Yu, P., Freed-Pastor, W. A., Abbondanza, D., Mehta, A., Gould, J., Lambden, C., Porter, C. B. M., Tsankov, A., Dionne, D., Waldman, J., Cuoco, M. S., Nguyen, L., Delorey, T., Phillips, D., Barth, J. L., Kem, M., Rodrigues, C., Ciprani, D., Roldan, J., Zelga, P., Jorgji, V., Chen, J. H., Ely, Z., Zhao, D., Fuhrman, K., Fropf, R., Beechem, J. M., Loeffler, J. S., Ryan, D. P., Weekes, C. D., Ferrone, C. R., Qadan, M., Aryee, M. J., Jain, R. K., Neuberg, D. S., Wo, J. Y., Hong, T. S., Xavier, R., Aguirre, A. J., Rozenblatt-Rosen, O., Mino-Kenudson, M., Castillo, C. F.-D., Liss, A. S., Ting, D. T., Jacks, T., and Regev, A. (2022) Single-nucleus and spatial transcriptome profiling of pancreatic cancer identifies multicellular dynamics associated with neoadjuvant treatment. *Nat Genet* 54, 1178–1191

12. Klein, L., Tu, M., Krebs, N., Urbach, L., Grimm, D., Latif, M. U., Penz, F., Blandau, A., Wu, X., Samuel, R. D., Küffer, S., Wegwitz, F., Chan, N., Aliar, K., Vyas, F., Kishore, U., Hessmann, E., Trumpp, A., Espinet, E., Papantonis, A., Khokha, R., Ellenrieder, V., Grünwald, B. T., and Singh, S. K. (2025) Spatial tumor immune heterogeneity facilitates subtype co-existence and therapy response in pancreatic cancer. *Nat Commun* 16, 335

13. Liudahl, S. M., Betts, C. B., Sivagnanam, S., Morales-Oyarvide, V., da Silva, A., Yuan, C., Hwang, S., Grossblatt-Wait, A., Leis, K. R., Larson, W., Lavoie, M. B., Robinson, P., Dias Costa, A., Väyrynen, S. A., Clancy, T. E., Rubinson, D. A., Link, J., Keith, D., Horton, W., Tempero, M. A., Vonderheide, R. H., Jaffee, E. M., Sheppard, B., Goecks, J., Sears, R. C., Park, B. S., Mori, M., Nowak, J. A., Wolpin, B. M., and Coussens, L. M. (2021) Leukocyte Heterogeneity in Pancreatic Ductal Adenocarcinoma: Phenotypic and Spatial Features Associated with Clinical Outcome. *Cancer Discov* 11, 2014–2031

14. Mi, H., Sivagnanam, S., Betts, C. B., Liudahl, S. M., Jaffee, E. M., Coussens, L. M., and Popel, A. S. (2022) Quantitative Spatial Profiling of Immune Populations in Pancreatic Ductal Adenocarcinoma Reveals Tumor Microenvironment Heterogeneity and Prognostic Biomarkers. *Cancer Res* 82, 4359–4372

15. de Souza, N., Zhao, S., and Bodenmiller, B. (2024) Multiplex protein imaging in tumour biology. *Nat Rev Cancer* 24, 171–191

16. Keren, L., Bosse, M., Marquez, D., Angoshtari, R., Jain, S., Varma, S., Yang, S.-R., Kurian, A., Van Valen, D., West, R., Bendall, S. C., and Angelo, M. (2018) A Structured Tumor-Immune Microenvironment in Triple Negative Breast Cancer Revealed by Multiplexed Ion

Beam Imaging. *Cell* 174, 1373–1387.e19

17. Han, G., Spitzer, M. H., Bendall, S. C., Fantl, W. J., and Nolan, G. P. (2018) Metal-isotope-tagged monoclonal antibodies for high-dimensional mass cytometry. *Nat Protoc* 13, 2121–2148

18. Bai, Y., Zhu, B., Oliveria, J.-P., Cannon, B. J., Feyaerts, D., Bosse, M., Vijayaragavan, K., Greenwald, N. F., Phillips, D., Schürch, C. M., Naik, S. M., Ganio, E. A., Gaudilliere, B., Rodig, S. J., Miller, M. B., Angelo, M., Bendall, S. C., Rovira-Clavé, X., Nolan, G. P., and Jiang, S. (2023) Expanded vacuum-stable gels for multiplexed high-resolution spatial histopathology. *Nat Commun* 14, 4013

19. Keren, L., Bosse, M., Thompson, S., Risom, T., Vijayaragavan, K., McCaffrey, E., Marquez, D., Angoshtari, R., Greenwald, N. F., Fienberg, H., Wang, J., Kambham, N., Kirkwood, D., Nolan, G., Montine, T. J., Galli, S. J., West, R., Bendall, S. C., and Angelo, M. (2019) MIBI-TOF: A multiplexed imaging platform relates cellular phenotypes and tissue structure. *Sci Adv* 5, eaax5851

20. Jiang, S., Chan, C. N., Rovira-Clavé, X., Chen, H., Bai, Y., Zhu, B., McCaffrey, E., Greenwald, N. F., Liu, C., Barlow, G. L., Weirather, J. L., Oliveria, J. P., Nakayama, T., Lee, I. T., Matter, M. S., Carlisle, A. E., Philips, D., Vazquez, G., Mukherjee, N., Busman-Sahay, K., Nekorchuk, M., Terry, M., Younger, S., Bosse, M., Demeter, J., Rodig, S. J., Tzankov, A., Goltsev, Y., McIlwain, D. R., Angelo, M., Estes, J. D., and Nolan, G. P. (2022) Combined protein and nucleic acid imaging reveals virus-dependent B cell and macrophage immunosuppression of tissue microenvironments. *Immunity* 55, 1118–1134.e8

21. Yeo, Y. Y., Cramer, P., Deisher, A., Bai, Y., Zhu, B., Yeo, W.-J., Shipp, M. A., Rodig, S. J., and Jiang, S. (2024) A Hitchhiker's guide to high-dimensional tissue imaging with multiplexed ion beam imaging. *Methods Cell Biol* 186, 213–231

22. Greenwald, N. F., Nederlof, I., Sowers, C., Ding, D. Y., Park, S., Kong, A., Houlahan, K. E., Varra, S. R., de Graaf, M., Geurts, V., Liu, C. C., Ranek, J. S., Voorwerk, L., de Maaker, M., Kagel, A., McCaffrey, E., Khan, A., Yeh, C. Y., Fullaway, C. C., Khair, Z., Bai, Y., Piyadasa, H., Risom, T., Delmastro, A., Hartmann, F. J., Mangiante, L., Sotomayor-Vivas, C., Schumacher, T. N., Ma, Z., Bosse, M., van de Vijver, M. J., Tibshirani, R., Horlings, H. M., Curtis, C., Kok, M., and Angelo, M. (2025) Temporal and spatial composition of the tumor microenvironment predicts response to immune checkpoint inhibition. *bioRxiv*,

23. Greenwald, N. F., Miller, G., Moen, E., Kong, A., Kagel, A., Dougherty, T., Fullaway, C. C., McIntosh, B. J., Leow, K. X., Schwartz, M. S., Pavelchek, C., Cui, S., Camplisson, I., Bar-Tal, O., Singh, J., Fong, M., Chaudhry, G., Abraham, Z., Moseley, J., Warshawsky, S., Soon, E., Greenbaum, S., Risom, T., Hollmann, T., Bendall, S. C., Keren, L., Graf, W., Angelo, M., and Van Valen, D. (2022) Whole-cell segmentation of tissue images with human-level performance using large-scale data annotation and deep learning. *Nat Biotechnol* 40, 555–565

24. Levine, J. H., Simonds, E. F., Bendall, S. C., Davis, K. L., Amir, E.-A. D., Tadmor, M. D., Litvin, O., Fienberg, H. G., Jager, A., Zunder, E. R., Finck, R., Gedman, A. L., Radtke, I., Downing, J. R., Pe'er, D., and Nolan, G. P. (2015) Data-Driven Phenotypic Dissection of AML Reveals Progenitor-like Cells that Correlate with Prognosis. *Cell* 162, 184–197

25. Chen, Z., Soifer, I., Hilton, H., Keren, L., and Jojic, V. (2020) Modeling Multiplexed Images

Journal Pre-proof

with Reveals Novel Tissue Microenvironments. *J Comput Biol* 27, 1204–1218

26. Arnold, B. F., Hogan, D. R., Colford, J. M., Jr, and Hubbard, A. E. (2011) Simulation methods to estimate design power: an overview for applied research. *BMC Med Res Methodol* 11, 94

27. Jeon, H., Xie, J., Jeon, Y., Jung, K. J., Gupta, A., Chang, W., and Chung, D. (2023) Statistical Power Analysis for Designing Bulk, Single-Cell, and Spatial Transcriptomics Experiments: Review, Tutorial, and Perspectives. *Biomolecules* 13,

28. Baker, E. A. G., Schapiro, D., Dumitrascu, B., Vickovic, S., and Regev, A. (2023) In silico tissue generation and power analysis for spatial omics. *Nat Methods* 20, 424–431

29. Brown, L. D., Cai, T. T., and DasGupta, A. (2001) Interval Estimation for a Binomial Proportion. *Statistical Science* 16, 101–133

30. Galon, J., Pagès, F., Marincola, F. M., Thurin, M., Trinchieri, G., Fox, B. A., Gajewski, T. F., and Ascierto, P. A. (2012) The immune score as a new possible approach for the classification of cancer. *J Transl Med* 10, 1

31. Wang, T.-T., Zhao, Y.-L., Peng, L.-S., Chen, N., Chen, W., Lv, Y.-P., Mao, F.-Y., Zhang, J.-Y., Cheng, P., Teng, Y.-S., Fu, X.-L., Yu, P.-W., Guo, G., Luo, P., Zhuang, Y., and Zou, Q.-M. (2017) Tumour-activated neutrophils in gastric cancer foster immune suppression and disease progression through GM-CSF-PD-L1 pathway. *Gut* 66, 1900–1911

32. Xue, R., Zhang, Q., Cao, Q., Kong, R., Xiang, X., Liu, H., Feng, M., Wang, F., Cheng, J., Li, Z., Zhan, Q., Deng, M., Zhu, J., Zhang, Z., and Zhang, N. (2022) Liver tumour immune microenvironment subtypes and neutrophil heterogeneity. *Nature* 612, 141–147

33. Yajuk, O., Baron, M., Toker, S., Zelter, T., Fainsod-Levi, T., and Granot, Z. (2021) The PD-L1/PD-1 Axis Blocks Neutrophil Cytotoxicity in Cancer. *Cells* 10,

34. Basnet, A., Landreth, K. M., Nohoesu, R., Santiago, S. P., Geldenhuys, W. J., Boone, B. A., and Liu, T. W. (2024) Targeting myeloperoxidase limits myeloid cell immunosuppression enhancing immune checkpoint therapy for pancreatic cancer. *Cancer Immunol Immunother* 73, 57

35. Fridlender, Z. G., Sun, J., Kim, S., Kapoor, V., Cheng, G., Ling, L., Worthen, G. S., and Albelda, S. M. (2009) Polarization of tumor-associated neutrophil phenotype by TGF-beta: “N1” versus “N2” TAN. *Cancer Cell* 16, 183–194

36. Ng, M. S. F., Kwok, I., Tan, L., Shi, C., Cerezo-Wallis, D., Tan, Y., Leong, K., Calvo, G. F., Yang, K., Zhang, Y., Jin, J., Liong, K. H., Wu, D., He, R., Liu, D., Teh, Y. C., Bleriot, C., Caronni, N., Liu, Z., Duan, K., Narang, V., Ballesteros, I., Moalli, F., Li, M., Chen, J., Liu, Y., Liu, L., Qi, J., Liu, Y., Jiang, L., Shen, B., Cheng, H., Cheng, T., Angeli, V., Sharma, A., Loh, Y.-H., Tey, H. L., Chong, S. Z., Iannacone, M., Ostuni, R., Hidalgo, A., Ginhoux, F., and Ng, L. G. (2024) Deterministic reprogramming of neutrophils within tumors. *Science* 383, eadf6493

37. Kwok, I., Becht, E., Xia, Y., Ng, M., Teh, Y. C., Tan, L., Evrard, M., Li, J. L. Y., Tran, H. T. N., Tan, Y., Liu, D., Mishra, A., Liong, K. H., Leong, K., Zhang, Y., Olsson, A., Mantri, C. K., Shyamsunder, P., Liu, Z., Piot, C., Dutertre, C.-A., Cheng, H., Bari, S., Ang, N., Biswas, S.

Journal Pre-proof

K., Koeffler, H. P., Tey, H. L., Larbi, A., Su, I.-H., Lee, B., St John, A., Chan, J. K. Y., Hwang, W. Y. K., Chen, J., Salomonis, N., Chong, S. Z., Grimes, H. L., Liu, B., Hidalgo, A., Newell, E. W., Cheng, T., Ginhoux, F., and Ng, L. G. (2020) Combinatorial Single-Cell Analyses of Granulocyte-Monocyte Progenitor Heterogeneity Reveals an Early Uni-potent Neutrophil Progenitor. *Immunity* 53, 303–318.e5

38. Clark, C. E., Hingorani, S. R., Mick, R., Combs, C., Tuveson, D. A., and Vonderheide, R. H. (2007) Dynamics of the immune reaction to pancreatic cancer from inception to invasion. *Cancer Res* 67, 9518–9527

39. Bayne, L. J., Beatty, G. L., Jhala, N., Clark, C. E., Rhim, A. D., Stanger, B. Z., and Vonderheide, R. H. (2012) Tumor-derived granulocyte-macrophage colony-stimulating factor regulates myeloid inflammation and T cell immunity in pancreatic cancer. *Cancer Cell* 21, 822–835

40. Ng, M., Cerezo-Wallis, D., Ng, L. G., and Hidalgo, A. (2025) Adaptations of neutrophils in cancer. *Immunity* 58, 40–58

Figure legends

Figure 1. Study cohort and multiplexed ion beam imaging workflow.

(A) Study design schematic depicting treatment-naïve pancreatic cancer patients (n=12) who underwent tissue sectioning (12 regions, 35 total fields of view) followed by adjuvant chemotherapy. Patient outcomes were tracked, resulting in two cohorts: those who relapsed (n=8) and those with no relapse to date (n=4). Created in BioRender. Yeung, J. (2025) https://BioRender.com/baxw1tg

(B) Multiplexed Ion Beam Imaging (MIBI) antibody panel comprising 27 markers organized into cell phenotype (lymphoid, myeloid, others) and functional markers.Created in BioRender. Yeung, J. (2025) https://BioRender.com/vvp3ilz

(C) MIBI experimental and computational workflow diagram showing: specimen preparation with metal-isotope conjugated antibodies, ion beam rastering across tissue samples, time-of-flight mass spectrometry for isotope detection, multiplexed image assembly, segmentation and feature extraction from cellular boundaries, iterative graph-based

Journal Pre-proof

clustering for cell type identification, cell type annotation using marker expression profiles, spatial projection with validation of tissue architecture, and downstream various distance-based analyses. Created in BioRender. Yeung, J. (2025) https://BioRender.com/p779w0j

(D) Representative images of pancreatic adenocarcinoma tissue: H&E stained section (left) and corresponding MIBI multiplex image (right) showing cytokeratin (magenta), CD11b (yellow), CD4 (green), and Histone H3 (gray).

Figure 2. Annotation and enrichment of PDAC cell populations.

(A) Spatial cell phenotyping visualization showing a multiplexed MIBI image (top) with cytokeratin (magenta), CD11b (cyan), CD16 (yellow), and Histone H3 (gray), alongside a cell type annotation map (bottom) with computationally identified cell populations represented in various colors.

(B) Heatmap of marker expression across identified cell types. The upper panel shows expression levels (Z-scores) of lineage markers with histogram of cell type counts. The lower panel displays functional marker expression across the identified cell populations. Color bars at bottom indicate different cell types.

(C) Cell type enrichment analysis comparing Relapse+ (top) versus Relapse- (bottom) patient samples, showing log2 fold enrichment for each cell type, represented by corresponding colors. Significance determined by Wilcoxon rank sum test of cell type proportion between relapse and non-relapse populations (*** = $p < 0.001$, ** = $p < 0.01$, * = $p < 0.05$).

(D) Infiltration of various immune cell species across tissue samples from different patients. Color stratifies patients who have relapsed versus those who have not.

Figure 3. Classification and enrichment of cell neighborhoods in PDAC TME.

(A) Cellular neighborhood classification workflow showing cell phenotype map (left) and corresponding cell neighborhood classification (right), with schematic representation of probabilistic topic modeling approach used to define spatial patterns and calculate neighborhood composition.

(B) Heatmap displaying distinct marker expression patterns within identified cellular neighborhoods. The upper panel shows lineage marker expression with histogram of neighborhood counts. The lower panel shows functional markers across different cellular neighborhood types. Color bar indicates neighborhood classifications.

(C) Log2 fold enrichment values for each identified cellular neighborhood in relapse-positive (Relapse+) versus relapse-negative (Relapse-) patients. Significance determined by Wilcoxon rank sum test of CN proportion between relapse and non-relapse populations (***: $p < 0.001$, **: $p < 0.01$, *: $p < 0.05$).

(D) Minimum distance from tumor neighborhood cells to cells from other neighborhoods. Median is calculated based on the median closest distance across all FOVs. Bars denote 25% and 75% interquartile range.

(E) Proportion of tumor to other neighborhood interfacing interactions based on Delaunay triangulation.

(F) Functional marker expression of non-tumor neighborhoods at the interface of tumor cell neighborhoods. Significance determined by Wilcoxon rank sum test (****: $p < 0.0001$, ***: $p < 0.001$, **: $p < 0.01$, *: $p <= 0.05$, ns: $p > 0.05$)

Figure 4. Analysis on neutrophils in PDAC TME based on tumor-cell distance.

(A) Cell-tumor distance measurement workflow: first, the tumor region masks were created from pathologist validated tumor annotation and keratin-mix marker image; then, the nearest tumor region was searched for each individual cell on a FOV, and a cell-tumor distance was calculated.

Journal Pre-proof

Journal Pre-proof

(B) The phenotype ratios at different tumor-cell distances were binned together and plotted against the tumor-cell distance to show the TME changes around tumor regions, data were splitted by patient status of relapsed and non-relapsed.

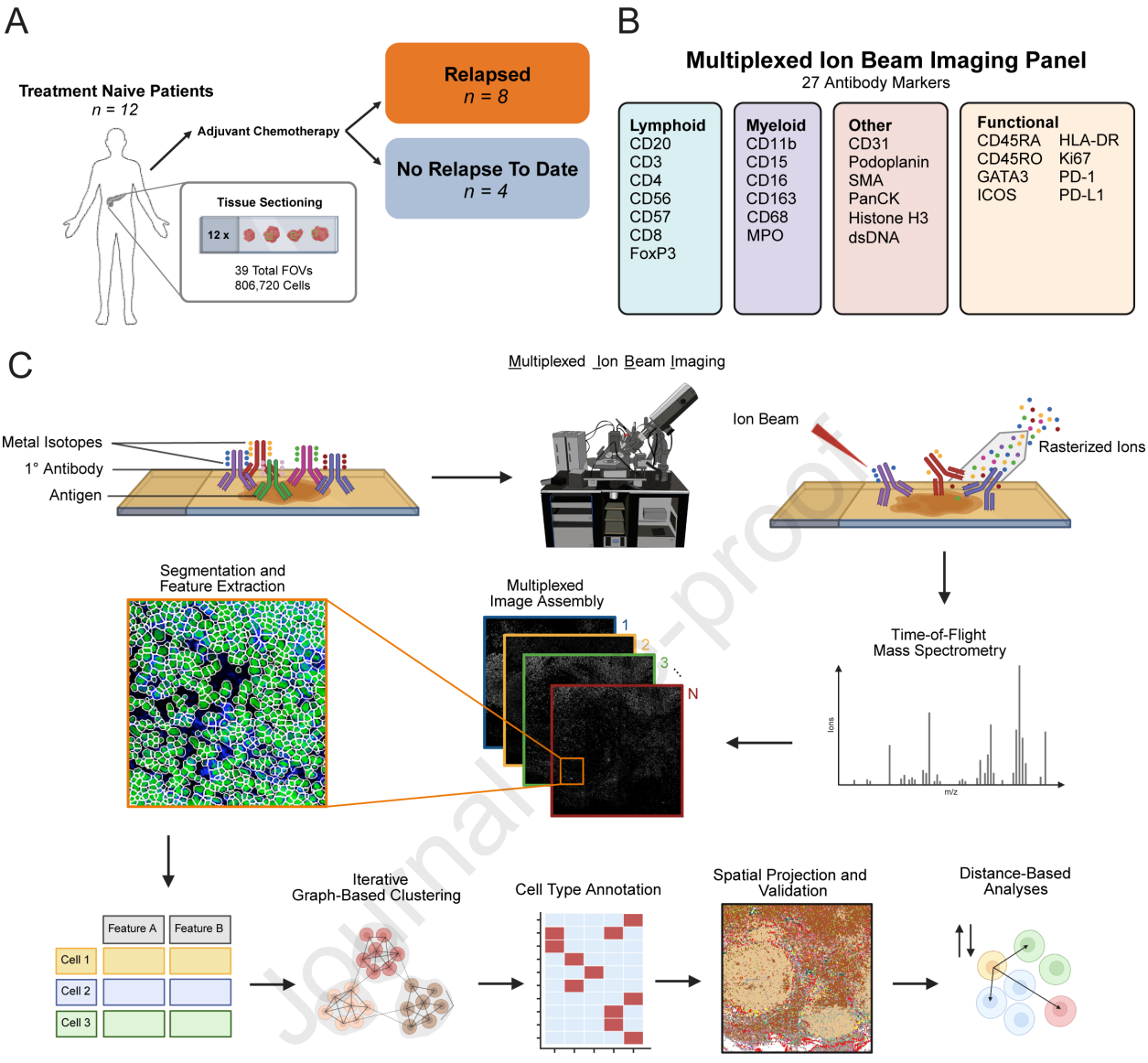
(C) Selected phenomarkers and functional markers of neutrophils in relapsed and non-relapsed patients. (****: $p < 0.0001$, ns: $p > 0.05$).

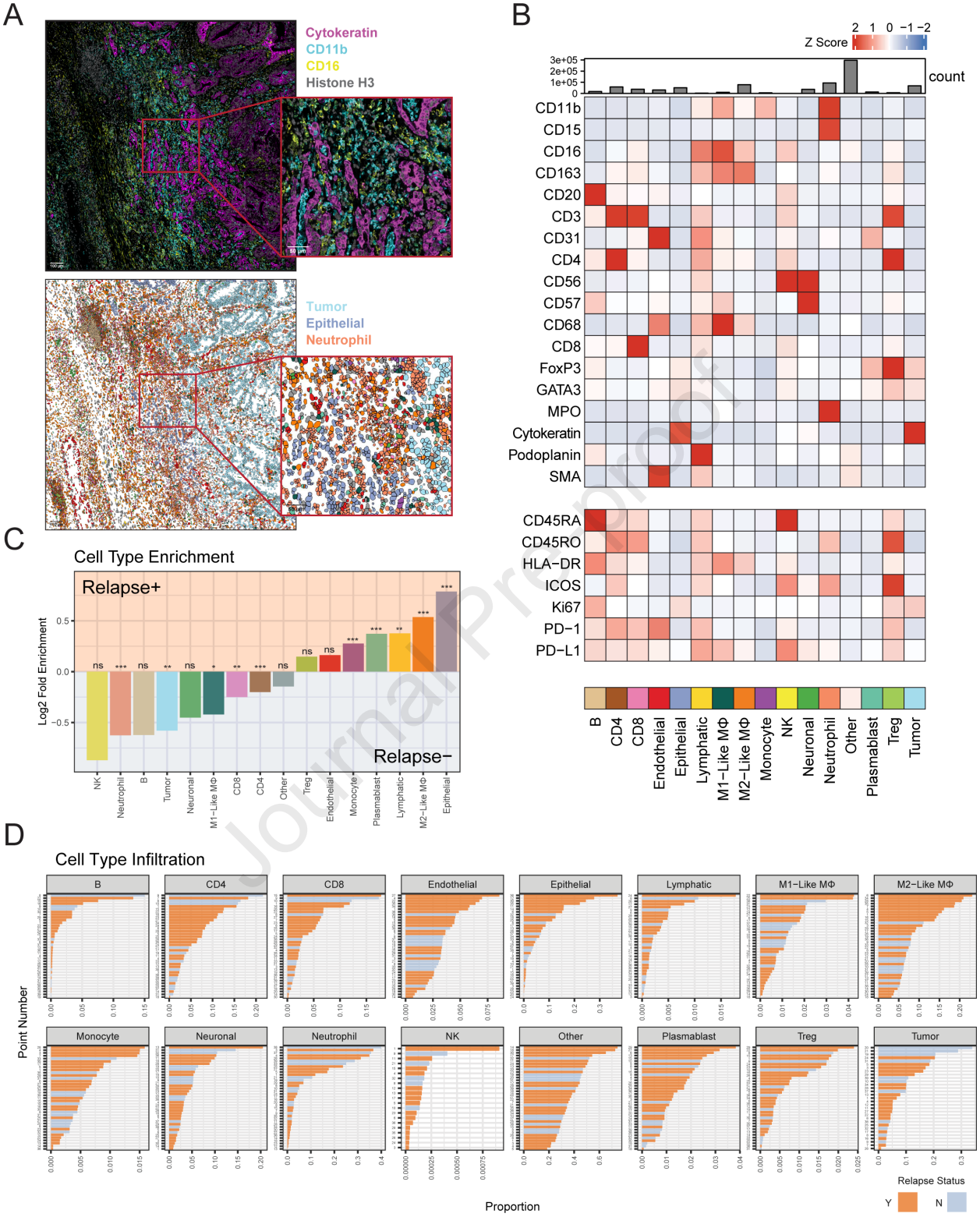
(D) Prediction accuracy of the random forest model based on PCA of neutrophil related features.

(E) The PCA loading matrix of principal components, or populations that contributed most significantly to the outcome of the random forest model. Columns of coefficients indicate the correlation of each individual marker toward the specific principal component, or population.

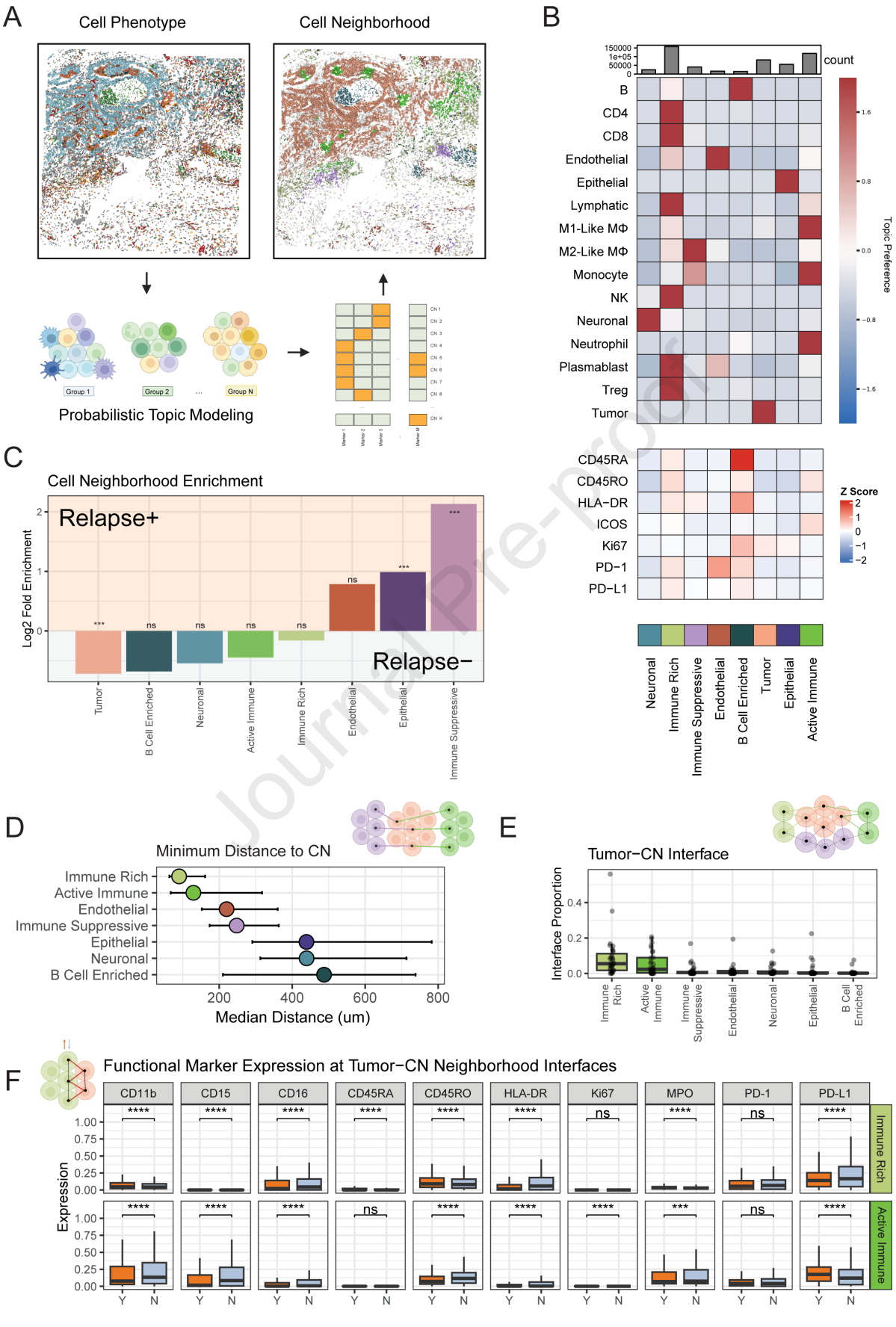
(F) Proposed model for the specialized neutrophil-associated signatures detected through the random forest model based on PCA of neutrophil related features and distance analysis.

Journal Pre-proof

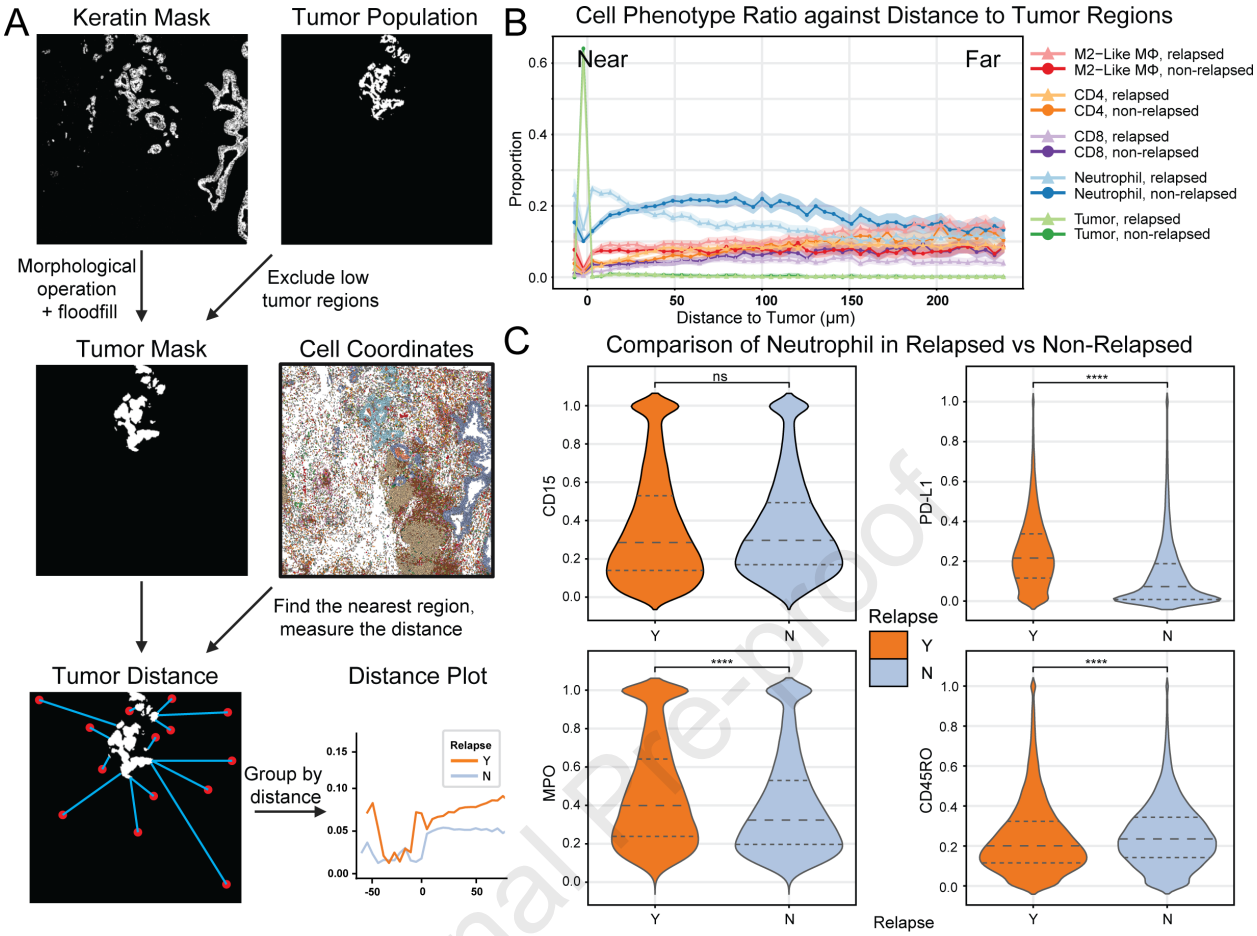

A
Treatment Naive Patients
n = 12
Adjuvant Chemotherapy
Relapsed
n = 8
No Relapse To Date
n = 4
Tissue Sectioning
12 x
39 Total FOVs
806,720 Cells
B
Multiplexed Ion Beam Imaging Panel
27 Antibody Markers
Lymphoid
CD20
CD3
CD4
CD56
CD57
CD8
FoxP3
Myeloid
CD11b
CD15
CD16
CD163
CD68
MPO
Other
CD31
Podoplanin
SMA
PanCK
Histone H3
dsDNA
Functional
CD45RA
CD45RO
GATA3
ICOS
HLA-DR
Ki67
PD-1
PD-L1
C
Multiplexed Ion Beam Imaging
Metal Isotopes
1° Antibody
Antigen
Ion Beam
Rasterized Ions
Segmentation and
Feature Extraction
Multiplexed
Image Assembly
1
2
3
N
Time-of-Flight
Mass Spectrometry
Ions
m/z
Feature A
Feature B
Cell 1
Cell 2
Cell 3
Iterative
Graph-Based Clustering
Cell Type Annotation
Spatial Projection and
Validation
Distance-Based
Analyses
D
Cytokeratin
CD11b
CD4
Histone H3

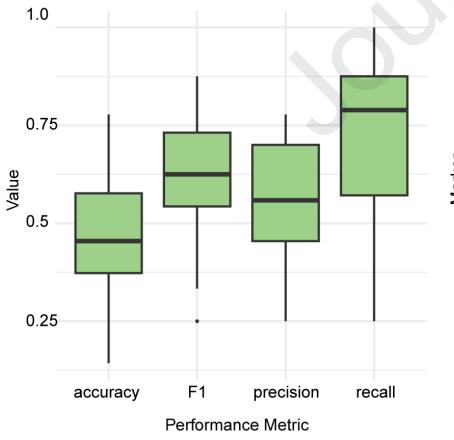


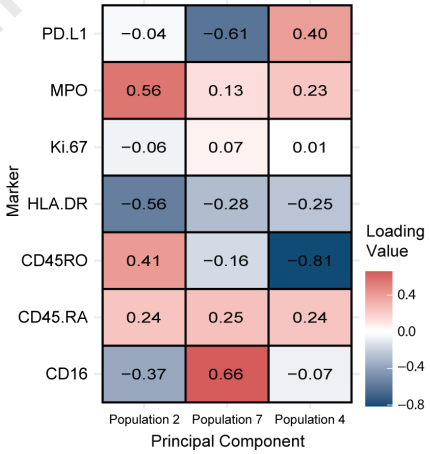
Journal Pre-proof

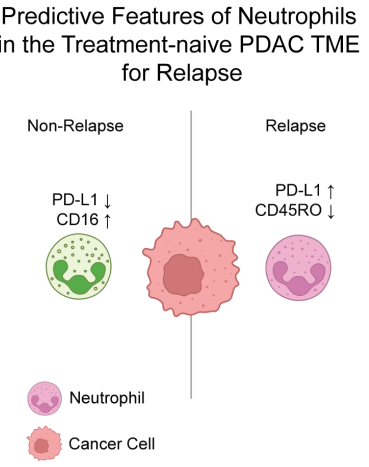


Journal Pre-proof









Journal Pre-proof

Journal Pre-proof

Spatial Proteomics Uncovers Immune Cell Neighborhoods and Tumor-Immune Interfaces in Pancreatic Ductal Adenocarcinoma

Highlights:

- Mapping and deciphering of the PDAC tumor microenvironment by spatial proteomics.
- Myeloid enrichment and cytotoxic CD8+ T cells depletion in relapsed patients.
- Identification of cell neighborhoods with frequent interactions with tumor regions.
- Neutrophil heterogeneity at the tumor–immune interface may relate to relapse status.

Journal Pre-proof

Spatial Proteomics Uncovers Immune Cell Neighborhoods and Tumor-Immune Interfaces in Pancreatic Ductal Adenocarcinoma

In Brief Summary:

The tumor microenvironment of pancreatic ductal adenocarcinoma (PDAC) was profiled through multiplexed ion beam imaging (MIBI), and linked to disease recurrence. Relapsed patients exhibited enrichment of immunosuppressive myeloid populations, and depletion of cytotoxic CD8+ T cells. Although immunogenic neighborhoods were present throughout, relapsed cases continued characteristic functional marker profiles at the tumor-immune interfaces. Analysis on neutrophils in the tumor buffer zone associates higher predicted relapse with PD-L1^{high}/CD45RO^{low} and lower relapse with CD16^{high}/PD-L1^{low} neutrophil profiles, highlighting potential recurrence-associated neutrophil states that require further validation.

Journal Pre-proof

Journal Pre-proof

Declaration of Interest Statement

☐ The authors declare that they have no known competing financial interests or personal relationships that could have appeared to influence the work reported in this paper.

☐ The author is an Editorial Board Member/Editor-in-Chief/Associate Editor/Guest Editor for this journal and was not involved in the editorial review or the decision to publish this article.

☒ The authors declare the following financial interests/personal relationships which may be considered as potential competing interests:

S.S. held a personal fellowship from BMS during this study with a grant provided to conduct experiments and also has research funding from Alchemab, has received speaker fees and travel grants from Astrazeneca, Novartis and Servier; and also conducts trials with Astrazeneca, Novartis, Roche, Genentech and BioNTech. S.J. is a co-founder of Elucidate Bio Inc, and serves on its Board of Directors and Scientific Advisory Board, and has received research support from Roche and Novartis unrelated to this work. The authors declare no other competing interests.

Journal Pre-proof